Scilight

Advanced Characterization

https://www.sciltp.com/journals/ac

Article

Probing Buried Interfaces and Phase Gradients in $MAPbI_3$ Films via Combined Back- and Surface-Incidence GIXRD

Liujiang Zhang [1,2,3,4,†], Guanhaojie Zheng [1,2,*,†], Zhenhuang Su [1], Zhen Wang [1], Chenyue Wang [1], Li Chen [1], Jianhua He [4,*] and Xingyu Gao [1,2,3,*]

[1] Shanghai Synchrotron Radiation Facility, Shanghai Advanced Research Institute, Chinese Academy of Sciences, Shanghai 201204, China
[2] Shanghai Institute of Applied Physics, Chinese Academy of Sciences, Shanghai 201800, China
[3] University of Chinese Academy of Sciences, Beijing 100049, China
[4] The Institute for Advanced Studies, Wuhan University, Wuhan 430072, China
* Correspondence: zhengguanhaojie@sari.ac.cn (G.Z.); hejianhua@whu.edu.cn (J.H.); gaoxy@sari.ac.cn (X.G.)
† These authors contributed equally to this work.

How To Cite: Zhang, L.; Zheng, G.; Su, Z.; et al. Probing Buried Interfaces and Phase Gradients in $MAPbI_3$ Films via Combined Back- and Surface-Incidence GIXRD. *Advanced Characterization* **2026**, *1*(1), 12–21.

Received: 2 February 2026
Revised: 10 March 2026
Accepted: 11 March 2026
Published: 31 March 2026

Abstract: Interfaces between the perovskite absorber and charge-transport layers play a critical role in determining the performance of planar perovskite solar cells (PSCs). However, the lack of non-destructive techniques capable of directly probing the microstructure of buried interfaces beneath perovskite films has significantly hindered a comprehensive understanding of their interfacial properties. Here, we employ flexible substrates to enable synchrotron-based grazing-incidence X-ray diffraction (GIXRD) measurements from the backside of the substrate, allowing direct investigation of buried interfaces. By combining back- and surface-incidence GIXRD, we construct a depth-resolved phase diagram spanning from the film surface to the buried interface in one-step deposited $MAPbI_3$ films. The film surface is dominated by a thin tetragonal perovskite layer, whereas a cubic phase gradually emerges with increasing depth, leading to phase coexistence within the film interior. Closer to the buried interface, the cubic phase progressively dominates, with the tetragonal phase completely disappearing at the interface. Meanwhile, high-resolution synchrotron X-ray diffraction measurements of $MAPbI_3$ powders at variable temperatures reveal that cubic and tetragonal phases can coexist, with their relative fractions strongly dependent on thermal history, despite the thermodynamic preference for the tetragonal phase at room temperature. The observed depth-dependent phase distribution in $MAPbI_3$ films is therefore attributed to an incomplete cubic-to-tetragonal phase transition during cooling after annealing, which becomes increasingly suppressed with depth due to substrate confinement. These findings provide new insights into the structure – performance relationship of one-step deposited $MAPbI_3$-based PSCs and demonstrate that back-incidence GIXRD is a powerful and broadly applicable tool for probing buried interfaces in thin-film systems.

Keywords: $MAPbI_3$ perovskite; back-incidence grazing incidence X-ray diffraction; depth dependent phase distribution

1. Introduction

Organometal halide perovskites have attracted tremendous attention in the field of photovoltaics due to their exceptional optoelectronic properties, including long carrier diffusion lengths, sharp absorption edges, high defect tolerance, and versatile fabrication routes [1–4]. To date, the certified power conversion efficiency (PCE) of

perovskite solar cells (PSCs) based on mixed organic cations and halide anions has reached over 27%, firmly establishing PSCs as one of the most promising photovoltaic technologies [5–9]. The continuous improvement in PSC performance over the past decade arises not only from the intrinsic advantages of perovskite materials but also from intensive efforts devoted to fabrication-process optimization and device heterostructure engineering [10–14].

It is widely recognized that achieving high-performance PSCs first requires the fabrication of high-quality perovskite films with minimal defects. In polycrystalline perovskite films, both the surface and the buried interface are intrinsically defect-rich regions that critically affect device efficiency and stability. Consequently, considerable attention has been devoted to defect passivation in both regions during film fabrication [15,16]. For instance, antisolvent treatment has become a standard practice for one-step deposited perovskite films to improve surface morphology and crystallinity, while interfacial engineering has proven to be an effective strategy for realizing high-quality perovskite films [10]. Film surfaces are readily accessible to a wide range of characterization techniques, facilitating effective process optimization and surface defect passivation [17–21]. The buried interface, despite being equally important in determining PSC efficiency and operational stability, has only later emerged as a focal point of intensive research [22–26]. A major challenge lies in the limited accessibility of buried interfaces beneath perovskite films using conventional characterization methods. In particular, crucial information regarding interfacial microstructures cannot be directly extracted from standard X-ray Diffraction (XRD) or synchrotron-based grazing-incidence X-ray diffraction (GIXRD) measurements, as the diffraction signals originating from the buried interface are hard to distinguish from those of the bulk film. To investigate buried interfaces in two-step spin-coated perovskite films and elucidate their structure–function relationships, Yang et al. employed a lift-off strategy that exposed submicrometer-scale extended defects and lead–halide inhomogeneities at the interface [27]. Similarly, Chen et al. applied GIXRD to the interface after mechanically peeling off Methylammonium lead triiodide ($CH_3NH_3PbI_3$: $MAPbI_3$) films [28]. However, such interface-exposure approaches are inherently destructive and may significantly alter or damage the native interfacial microstructures that are originally bonded to the substrate.

On the other hand, the surface and interface of a thin film represent regions where bulk crystal symmetry is broken, and their microstructures can differ substantially from those of the film interior. Moreover, halide perovskites are well known for exhibiting rich phase behavior, including phase transitions not only among different perovskite crystal structures but also from optically active perovskite phases to undesirable non-perovskite phases. For example, $MAPbI_3$ undergoes a sequence of temperature-driven phase transitions: orthorhombic ($T < -103$ °C), tetragonal (-103 °C $< T <$ 56 °C), and cubic ($T >$ 56 °C) [29–31]. Because the tetragonal-to-cubic transition temperature is close to room temperature, several studies have reported that the cubic phase can be stabilized at room temperature under certain conditions [32–34]. Given that solution-processed perovskite films are typically annealed at temperatures exceeding 100 °C and subsequently cooled to room temperature, it is reasonable to expect a complex depth-dependent phase distribution in $MAPbI_3$ films, rather than a uniform crystal phase throughout the thickness. Such phase heterogeneity may coexist with variations in defect density from the surface to the buried interface. As the efficiency and stability of PSCs are highly sensitive to the phase composition and microstructure of the perovskite layer, elucidating the depth-dependent phase distribution within perovskite films is therefore critical for a deeper understanding of device performance.

In this study, we employ a non-destructive back-incidence GIXRD to probe the buried interfaces of one-step deposited $MAPbI_3$ perovskite films on flexible substrates. By combining this with conventional surface-incident GIXRD, we uncover a depth-dependent structural gradient at room temperature. The film surface is tetragonal, the buried interface is predominantly cubic, and both phases coexist in the interior. This distribution is attributed to an incomplete cubic-to-tetragonal phase transition during cooling after annealing, which becomes increasingly suppressed from the free surface toward the substrate-bounded interface.

2. Experimental Section/Methods

Materials: SnO_2 colloid precursors (tin (iv) oxide, 15% in H_2O colloidal dispersion) were purchased from Alfa Aesar Chemical Co., Ltd. in Shanghai, China. N, N-dimethylformamide (DMF), chlorobenzene (CB), dimethyl sulfoxide (DMSO) used in this study were all bought from Sigma-Aldrich Trading Co., Ltd. in Shanghai, China. Lead iodine (PbI_2), methylammonium iodide (MAI) and $MAPbI_3$ single crystal powders were purchased from Xi'an Polymer Light Technology Corp. Ltd. in Xi'an, China. Indium Tin Oxide (ITO), polyethylene terephthalate (PET) substrates and neutral detergent were purchased from Youxuan New Energy Technology Corp., Ltd. in Yingkou, Liaoning province, China.

SnO_2 colloid precursor solutions: The commercial solution was used after being diluted using deionized water with a V_{SnO2}: V_{dw} ratio of 1:5.

Perovskite precursor solutions: The perovskite precursor solution was prepared by dissolving 461 mg lead iodide (PbI_2) and 159 mg methylammonium iodide (MAI) powder in mixed solvents of 700 μL N, N-dimethyl-formamide (DMF) and 78 μL dimethyl sulfoxide (DMSO). The prepared precursor solution was then kept on a hot plate at 60 °C for hours to promote the dissolution, then the solution was cooled down to room temperature.

Samples fabrication: The as-received flexible substrates (PET/ITO, A4-size) were firstly cut into pieces with a size of 15 mm×13 mm. All the substrates, including rigid glass/ITO substrates, were washed by distilled water, neutral detergent anhydrous ethanol, and isopropanol in turn. The substrates were then dried using N_2 and treated by UV/O_3 for 15 min before use. The diluted SnO_2 solution (SnO_2:H_2O = 1:5) was subsequently spin-coated onto the substrate at 3000 r.p.m. for 30 s and annealed at 100 °C for 30 min in air. Before transferring to a N_2-filled glovebox, another 10 min of UV/O_3 treatment was conducted to improve surface wettability. To fabricate $MAPbI_3$ films using a one-step method in the glovebox, perovskite precursor solutions were deposited onto ITO/SnO_2 substrates by spin coating at 3000 r.p.m. for 30 s, and CB anti-solvent was dropped upon the film during the 15-16th s. Subsequently, the as-prepared samples were annealed at 100 °C for 10 min. As a special note, special vacuum cupules were used for spin coating of perovskite films on PET flexible substrates. All samples in this work are based on PET flexible substrates unless otherwise specified.

Samples Characterizations: GIXRD: This work mainly makes use of GIXRD characterization, which was performed at the BL14B1 end station at the Shanghai Synchrotron Radiation Facility (SSRF) with a photon energy of 10 keV (wavelength = 1.2398 Å) [35]. As the sample placed at different incidence angles from 0.1° to 2.5° in the optical path and two-dimensional GIXRD images were collected by a MarCCD 225 detector at a vertical distance of ~ 300 mm from the sample with an exposure time of 30 s. The 2D GIXRD patterns were analyzed using the FIT2D software and displayed in scattering vector q coordinates with $q = 4\pi\sin\theta/\lambda$ (θ is half of the diffraction angle and λ is wavelength of incident X-ray). The scattering vector q was calibrated by using powder diffraction from LaB6 sample before the GIXRD measurements. In this work, besides GIXRD measured with X-ray incident on the surface of the perovskite films, GIXRD was also carried out with X-ray incident on the back of the substrate, i.e., *Back-Incidence GIXRD.* In such a case, the sample was turned upside down with the X-ray passing through the PET flexible substrate before reaching the perovskite films, as illustrated in Figure 1c.

High-Resolution X-ray powder Diffraction (XPD): The high-resolution XPD experiments were performed at the beamline BL14B1 as well. An incident photon energy of 18 keV was used corresponding to a wavelength of λ = 0.6887Å [35]. The powder sample was loaded in a capillary tube and its temperature was controlled by a custom-made heater system in a range of 26−100 °C. During the heating up to 100 °C and then cooling down to room temperature process, XPD measurements of the sample were carried out at selected constant temperatures by using a line detector. After the sample cooling down to room temperature for 20 min, the capillary with the sample was put into a refrigerator at ~0 °C for 2 min and then for one more XPD measurement.

Scanning electron microscopy (SEM): The SEM images were measured by field emission scanning electron microscope. The ZEISS GeminiSEM 300 was manufactured by Carl Zeiss Co., Ltd., Tokyo, Japan.

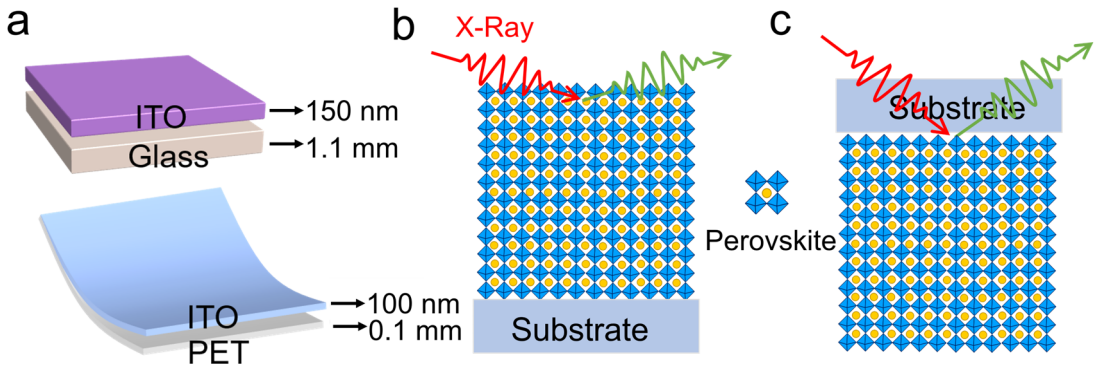

Figure 1. (**a**) Schematic illustrations of ITO and flexible PET substrates used in this study; Schematic geometry of GIXRD with X-ray incident on the film surface (**b**) and on the back of the substrate (**c**).

3. Results and Discussions

3.1. Morphologies of the Fabricate Films

To confirm that the flexible substrate does not compromise film morphology, we compare scanning electron microscope (SEM) images of perovskite films on indium tin oxide (ITO) glass and polyethylene terephthalate (PET)

(Figure S1). Both films exhibit nearly identical, compact, and pinhole-free morphologies with a uniform mixture of intergrown large and small grains. This demonstrates that film formation on PET yields morphological quality.

3.2. Methodology

To investigate the depth-dependent microstructure evolution in perovskite films, we employed GIXRD in two complementary geometries: conventional surface-incidence and back-incidence through the flexible substrate. Figure 1a illustrates the substrate structures: a flexible substrate comprising 100 nm ITO on 0.1 mm PET, compared to a standard 150 nm ITO on 1.1 mm glass. Figure 1b,c shows the corresponding GIXRD geometries. In surface-incidence mode, varying the incident angle probes different depths within the film. The back-incidence geometry operates on the same principle but requires a larger incident angle to penetrate the substrate layers. To ensure experimental reproducibility and address the inherent flexibility of the PET substrate, we first fixed the substrate onto a glass slide during sample preparation to maintain flatness, and then carefully removed it prior to measurement. During GIXRD data acquisition, the sample was securely mounted using vacuum adsorption to maintain sufficient flatness across the film region, thereby preventing any deviation in the incidence angle caused by substrate bending. In addition, the sample surface was leveled through a precise alignment procedure before measurement to ensure good parallelism with the instrument reference plane.To validate this approach, Figure S2 shows the 2D GIXRD pattern from a silver film on the same flexible substrate with an incident angle of 2.0° on surface in (a) and 3.0° on the back of the film in (b), respectively. It is clear that GIXRD is able to detect signals from both the (111) plane of Ag films at $q \approx 26$ nm^{-1} [36] and the substrate.

3.3. High-Resolution X-Ray Powder Diffraction of $MAPbI_3$ Single Crystal Powder

High-resolution X-ray powder diffraction (XPD) of $MAPbI_3$ single-crystal powder was first performed at varied temperatures to identify the characteristic peaks of its tetragonal and cubic phases (Figure 2). At room temperature, the pristine sample shows three distinct peaks at approximately 19.82, 19.93, and 20.00 nm^{-1} (Figure 2a). Upon heating to 60 °C (above the ~56 °C phase transition temperature), only the central peak at ~19.93 nm^{-1} remains (Figure 2b), which shifts slightly with further heating to 100 °C due to thermal lattice expansion (Figure 2c). This identifies the peaks at 19.82 and 20.00 nm^{-1} as belonging to the tetragonal phase and the peak at 19.93 nm^{-1} to the cubic phase. Specifically, the tetragonal peaks correspond to the (004) and (220) planes, while the cubic peak corresponds to the (002) plane [37]. This assignment is confirmed by the cooling cycle in Figure 2d–f. Cooling from 100 °C to 60 °C yields a single cubic peak (Figure 2d) at 60 °C. Subsequent cooling to room temperature results in a spectrum dominated by a broad cubic peak at 19.93 nm^{-1}, with only minor tetragonal features at 19.82 nm^{-1} and 20.00 nm^{-1} (Figure 2e), indicating an incomplete cubic to tetragonal phase transition by natural cooling to room temperature. Only after cooling down to 0 °C (Figure 2f) does the material fully transform into the pure tetragonal phase with two sharp peaks at 19.82 and 20.00 nm^{-1} without any sign of cubic phase. Even though the tetragonal phase is favorable at room temperature, these results conclusively demonstrate that both phases can coexist in $MAPbI_3$ with their relative proportions dictated by thermal history. Given that single-crystal powders represent an ideal, substrate-free system exhibiting thermodynamic equilibrium phase transition behavior, their diffraction data cannot be directly equated with the phase behavior of thin films influenced by interfacial interactions and stress. Therefore, in the discussion of this paper, we employ temperature-dependent powder diffraction data as an important reference benchmark to aid in understanding the substrate-modulated phase coexistence behavior in $MAPbI_3$ thin films, thereby providing deeper insight into their distinctive phase transition characteristics.

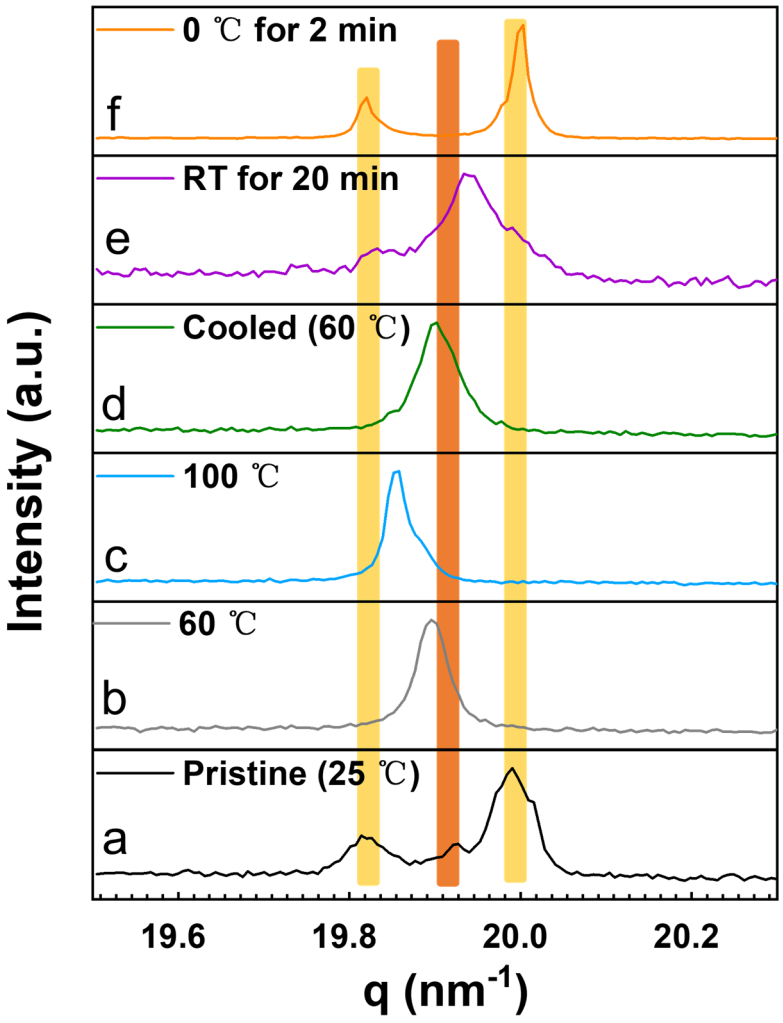

Figure 2. XPD patterns of $MAPbI_3$ single crystal powders at varied temperatures.

3.4. GIXRD of the $MAPbI_3$ films

To probe the depth-dependent microstructure near the surface region of a one-step deposited $MAPbI_3$ film, GIXRD measurements were performed at various incident angles. The 2D pattern at a 2.0° incident angle (Figure 3a) shows a bright diffraction ring at $q \approx 10.0$ nm^{-1}, indicating high crystallinity from the surface into the film interior (a weaker ring is visible at 0.1° in Figure S3). The radial integration of the pattern in Figure 3a was fitted with three Gaussian peaks at 9.85, 9.95, and 10.01 nm^{-1} (Figure 3b). By comparison with the reference data in Figure 2, these are assigned to the tetragonal (002), cubic (001), and tetragonal (110) planes, respectively [38]. This preliminary analysis reveals a film interior dominated by the cubic phase. A detailed depth profile is shown in Figure 3c–e, which compile radial integration plots from surface-incidence GIXRD at different angles. At highly surface-sensitive angles (0.1° and 0.2°), the spectra are best fitted by only the two tetragonal-phase peaks (yellow bars). At larger angles (>0.2°), which probe deeper, all three peaks (tetragonal and cubic, marked by yellow and brown bars) are present. It is also noticed that at grazing incident angles smaller than 0.6° all the peak positions are at larger q than those with larger incident angles. The difference present between the surface and the interior should be due to the fact that the atoms in the surface region are less bounded. To conclude, the key finding from the GIXRD results is that the film surface is purely tetragonal, while the cubic phase emerges and coexists with the tetragonal phase within the film interior.

For comparison, we also performed front-incidence angle-dependent GIXRD measurements on $MAPbI_3$ films deposited on ITO glass substrates. The results, shown in Figure S4, exhibit consistent peak shapes, indicating the presence of phase coexistence in these films as well. This demonstrates that the phase distribution characteristics in the surface region are not unique to PET flexible substrates, but are also present in films fabricated on conventional rigid substrates.

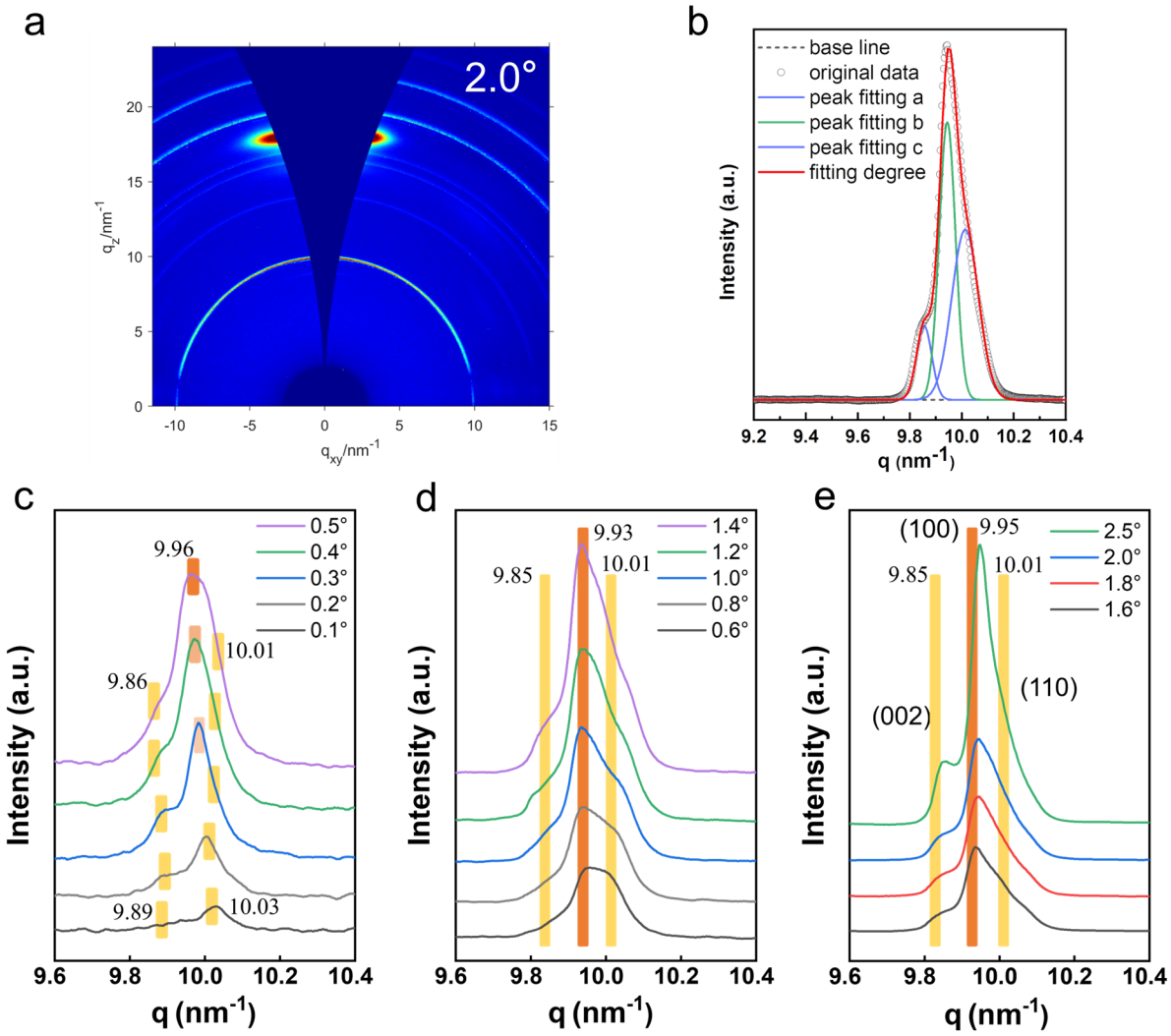

Figure 3. (**a**) The 2D GIXRD pattern with an incident angle of 2.0° on a one-step deposited $MAPbI_3$ film surface; (**b**) the Gaussian fitting of the radial integration plot of the 2D GIXRD pattern in (**a**); (**c**–**e**) the radial integration plots of 2D GIXRD patterns near q = 10.0 nm^{-1} with different incident angles on the film surface.

To complement the surface analysis, we employed back-incidence GIXRD to probe the microstructure from the buried interface upward of a one-step deposited $MAPbI_3$ film (Figure 4). Due to attenuation through the PET substrate, the characteristic perovskite diffraction ring at q ≈ 10 nm^{-1} is faint at a 1.2° incident angle (Figure S5a) and only becomes prominent at 3.0° (Figure S5b). The radial integration plots for incident angles between 1.0° and 3.0° are shown in Figure 4a–c. All spectra are fitted with three Gaussian peaks, corresponding to the tetragonal (yellow bars) and cubic (brown bar) phases. Critically, for the most interface-sensitive angles (<1.1°), only the cubic phase peak is present. This indicates a purely cubic phase at the buried interface, with the tetragonal phase emerging deeper in the film interior. Combined with the results from Figure 3, these data establish a depth-dependent phase gradient: a tetragonal surface, a cubic buried interface, and a mixed-phase interior.

In the following, a more quantitative depth-dependent phase diagram is constructed from the relative diffraction intensities of the cubic (black) and tetragonal (red) phases, plotted as functions of the incident angle (Figure 5). The intensities, derived from Gaussian fits to the spectra in Figures 3c–e and 4a–c, represent the cubic (001) peak and the sum of the tetragonal (002) and (110) peaks. In the surface-incidence data (Figure 5a), only the tetragonal phase is detected at angles below 0.3°, confirming a pure, thin surface layer. Between 0.3° and 1.0°, the cubic phase appears and its intensity gradually increases, though it remains weaker than the tetragonal phase. Beyond 1.0°, the intensities of both phases stabilize, indicating a constant mixed-phase composition in the bulk. The back-incidence data (Figure 5b) reveal a complementary trend at the buried interface. At the most interface-sensitive angles (1.0° and 1.1°), only the cubic phase is present. From 1.2° to 2.4°, the tetragonal phase intensity grows as the cubic phase diminishes, after which both intensities plateau, signifying the mixed-phase interior. The sharper transition from pure tetragonal to the mixed-phase region at the surface (Figure 5a), compared to the more

gradual evolution from the cubic interface (Figure 5b), suggests that the pure tetragonal surface layer may be thinner than the pure cubic layer at the buried interface.

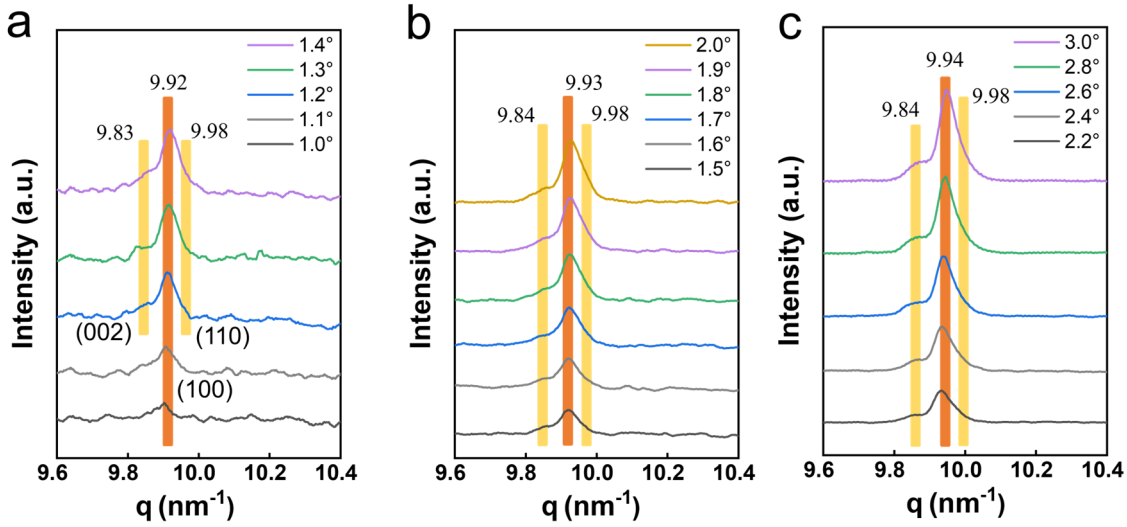

Figure 4. (**a**–**c**) The radial integration plots of 2D GIXRD patterns around q = 10 nm^{-1} with different incident angles on the back side of the substrate.

In summary, the depth-dependent phase diagram in $MAPbI_3$ films is schematized in Figure 5c. This distribution results from an incomplete cubic-to-tetragonal transition during cooling after annealing. Atoms at the substrate-buried interface are highly constrained, which suppresses the transition, leaving a predominantly cubic phase. In contrast, atoms at the free surface are minimally constrained, allowing the transition to proceed to completion, forming a pure tetragonal phase. Within the film interior, a gradient of constraint leads to a coexistence of both phases, with their relative concentrations varying continuously with depth.

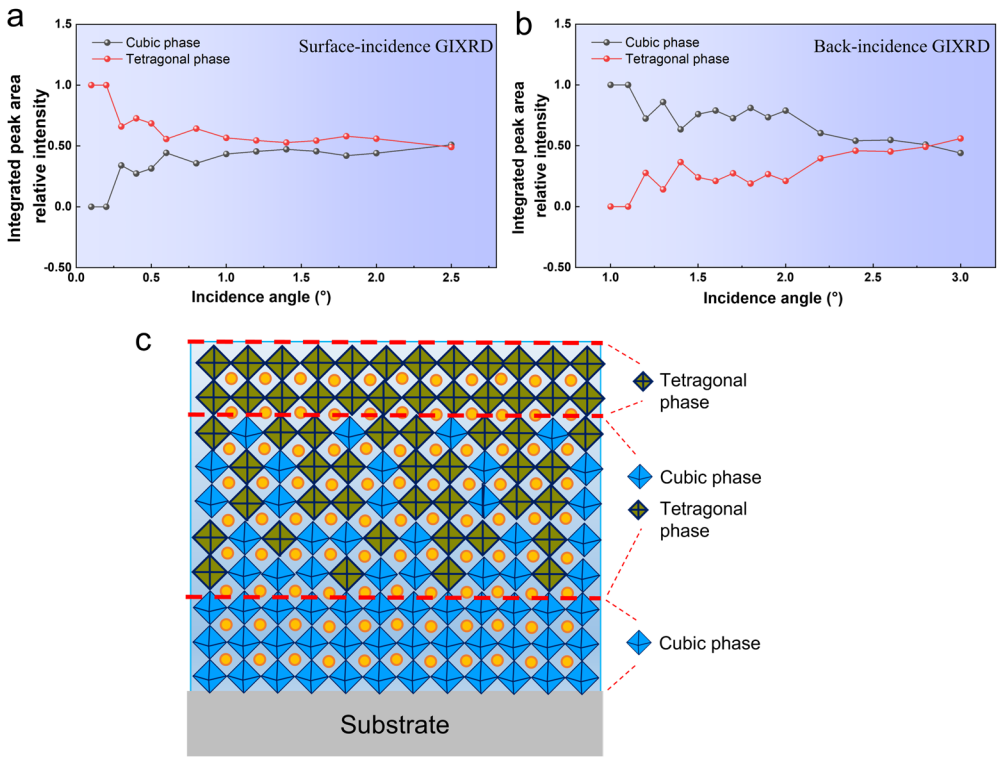

Figure 5. Depth-dependent phase analysis of $MAPbI_3$ films. (**a**) Relative diffraction intensities of the cubic (black) and tetragonal (red) phases as functions of the X-ray incident angle for surface-incidence GIXRD. (**b**) Corresponding phase intensities as functions of incident angle for back-incidence GIXRD through the substrate. (**c**) Schematic illustration of the phase distribution at room temperature (thicknesses are not to scale).

4. Conclusions

In conclusion, we have demonstrated the use of back-incidence GIXRD as a powerful, non-destructive method for probing the buried interface in perovskite films. By combining this technique with conventional surface-incidence GIXRD, we revealed a distinct depth-dependent phase gradient in one-step deposited $MAPbI_3$ films. A pure tetragonal phase was identified at the surface, a pure cubic phase at the buried interface, and a mixed-phase region in the film interior. This distribution is attributed to a kinetically hindered cubic-to-tetragonal transition upon cooling, which is suppressed at the substrate-constrained interface but proceeds fully at the free surface. These findings offer a deeper understanding of microstructure evolution in perovskites and establish back-incidence GIXRD as a valuable tool for investigating buried interfaces in a wide range of thin-film systems.

5. Outlook

This study revealed the depth-dependent phase distribution characteristics of $MAPbI_3$ films under dark and room-temperature conditions. However, under real operating conditions, factors such as illumination, temperature, and atmosphere may drive further phase structure evolution. Previous studies have shown that tetragonal and cubic perovskites exhibit fundamental differences in charge carrier transport, band structure, and thermodynamic stability—differences that directly determine the ultimate device efficiency and long-term operational stability [39]. Future research should focus on the following two directions: (1) conducting in-situ GIXRD characterization under controlled environments to track the evolution of phase structure and its depth distribution under external stimuli in real time; and (2) establishing a combined platform for controlled-environment and device performance characterization, aiming to quantitatively establish the structure–property relationship between specific phase composition and device efficiency/stability.

Supplementary Materials

The additional data and information can be downloaded at: https://media.sciltp.com/articles/others/2603311441027783/AC-26020007-Supplementary-Materials.pdf. Figure S1: The SEM images of $MAPbI_3$ thin films prepared on (a) a ITO glass substrate and (b) a PET flexible substrate, respectively; Figure S2: The 2D GIXRD patterns of a Ag film at incident angles of (a) 2.0° on the film surface and (b) 3.0°on the back of its substrate, respectively; Figure S3: The 2D GIXRD patterns at an incident angle of 0.1°on the film surface; Figure S4: Radial integration plots of 2D GIXRD patterns at $q \approx 10.0$ nm^{-1} for the film surface prepared on ITO glass under different incident angles; Figure S5: The 2D GIXRD patterns at incident angles of (a) 1.2° and (b) 3.0° on the back of the substrate, respectively.

Author Contributions

L.Z. and G.Z. contributed equally to this work. L.Z. and G.Z.: Conceptualization, Methodology, Data curation, Writing—original draft preparation; Z.S., Z.W., C.W. and L.C.: Formal Analysis, Validation, Methodology; G.Z., J.H., X.G.: Conceptualization, Supervision, Writing—Review & Editing, Funding Acquisition. All authors have read and agreed to the published version of the manuscript.

Funding

This research was funded by the Natural Science Foundation of China 12575354, the Shanghai Science and Technology Commission Program (25DZ3001901), and the Shanghai Pilot Program for Basic Research-Chinese Academy of Science, Shanghai Branch (JCYJ-SHFY-2022-002). This work was also supported by the Science and Technology Major Project of Hubei Province in China (2021AFB001). This work was also supported by the Youth Innovation Promotion Association of the Chinese Academy of Sciences (2023305).

Institutional Review Board Statement

Not applicable.

Informed Consent Statement

Not applicable.

Data Availability Statement

The authors declare that the data supporting the findings of this study are available within the paper and its Supplementary Information files. Source data are available from the corresponding author upon request.

Acknowledgments

The authors thank the beamline BL14B1 at Shanghai Synchrotron Radiation Facility (SSRF) for providing the beam time (https://cstr.cn/31124.02.SSRF.BL14B1). The authors thank the SSRF of BL03HB (https://cstr.cn/31124.02.SSRF.BL03HB) for the assistance on GIXRD measurements. The authors would also thank the SSRF of The Experimental Assist System (https://cstr.cn/31124.02.SSRF.LAB).

Conflicts of Interest

The authors declare no conflict of interest.

Use of AI and AI-Assisted Technologies

During the preparation of this work, we used AI DeepSeek to refine and polish the English grammar. After using this service, we reviewed and edited the content as needed and take full responsibility for the content of the published article.

References

1. Shi, D.; Adinolfi, V.; Comin, R.; et al. Low trap-state density and long carrier diffusion in organolead trihalide perovskite single crystals. *Science* **2016**, *347*, 519.
2. De Wolf, S.; Holovsky, J.; Moon, S.J.; et al. Organometallic halide perovskites sharp optical absorption edge and its relation to photovoltaic performance. *J. Phys. Chem. Lett.* **2014**, *5*, 1035.
3. Chu, W.; Zheng, Q.; Prezhdo, O.V.; et al. Low-frequency lattice phonons in halide perovskites explain high defect tolerance toward electron-hole recombination. *Sci. Adv.* **2020**, *6*, eaaw7453.
4. Jamal, M.S.; Bashar, M.S.; Hasan, A.K.M.; et al. Fabrication techniques and morphological analysis of perovskite absorber layer for high-efficiency perovskite solar cell: A review. *Renew. Sust. Energ. Rev.* **2018**, *98*, 469.
5. Jeong, M.; Choi, I.W.; Go, E.M.; et al. Stable perovskite solar cells with efficiency exceeding 24.8% and 0.3-V voltage loss. *Science* **2020**, *369*, 1615.
6. Jeong, J.; Kim, M.; Seo, J.; et al. Pseudo-halide anion engineering for α-$FAPbI_3$ perovskite solar cells. *Nature* **2021**, *592*, 381.
7. Min, H.; Lee, D.Y.; Kim, J.; et al. Perovskite solar cells with atomically coherent interlayers on SnO_2 electrodes *Nature* **2021**, *598*, 444.
8. Xiong Z.; Zhang Q.; Cai K.; et al. Homogenized chlorine distribution for >27% power conversion efficiency in perovskite solar cells. *Science* **2025**, *390*, 638.
9. National Renewable Energy Laboratory (NREL). Best Research-Cell Efficiency Chart. Available online: https://www.nrel.gov/pv/cell-efficiency.html (accessed on 1 February 2026).
10. Taylor, A.D.; Sun, Q.; Goetz, K.P.; et al. A general approach to high-efficiency perovskite solar cells by any antisolvent. *Nat. Commun.* **2021**, *12*, 1878.
11. Li, H.; Zhou, J.; Tan, L.; et al. Sequential vacuum-evaporated perovskite solar cells with more than 24% efficiency. *Sci. Adv.* **2022**, *8*, eabo7422.
12. Wang, Q.K.; Wang, R.B.; Shen, P.F.; et al Energy level offsets at lead halide perovskite/organic hybrid interfaces and their impacts on charge separation. *Adv. Mater. Interfaces* **2015**, *2*,1400528.
13. Qin, M.; Chan, P.F.; Lu, X. A systematic review of metal halide perovskite crystallization and film formation mechanism unveiled by In-situ GIWAXS. *Adv. Mater.* **2021**, *33*, e2105290.
14. Aydin, E.; De Bastiani, M.; De Wolf, S. Defect and contact passivation for perovskite solar cells. *Adv. Mater.* **2019**, *31*, e1900428.
15. Stolterfoht, M.; Wolff, C.M.; Márquez, J.A.; et al. Visualization and suppression of interfacial recombination for high-efficiency large-area pin perovskite solar cells. *Nat. Energy* **2018**, *3*, 847.
16. Shao, S.; Loi, M.A. The role of the interfaces in perovskite solar cells. *Adv. Mater. Interfaces* **2019**, *7*, 1901469.
17. Jiang, Q.; Zhao, Y.; Zhang, X.; et al. Surface passivation of perovskite film for efficient solar cells. *Nat. Photonics* **2019**, *13*, 460.
18. Chen, R.; Wang, Y.; Nie, S.; et al. Sulfonate-assisted surface iodide management for high-performance perovskite solar cells and modules. *J. Am. Chem. Soc.* **2021**, *143*, 10624.

19. Li, Z.; Li, B.; Wu, X.; et al. Organometallic-functionalized interfaces for highly efficient inverted perovskite solar cells. *Science* **2022**, *376*, 416.
20. Azmi, R.; Ugur, E.; Seitkhan, A.; et al. Damp heat-stable perovskite solar cells with tailored-dimensionality 2D/3D heterojunctions. *Science* **2022**, *376*, 73.
21. Jiang, Q.; Tong, J.; Xian, Y.; et al. Surface reaction for efficient and stable inverted perovskite solar cells. *Nature* **2022**, *611*, 278.
22. Xu, H.; Miao, Y.; Wei, N.; et al. CsI enhanced buried interface for efficient and UV-robust perovskite solar cells. *Adv. Energy Mater.* **2021**, *12*, 2103151.
23. Chen, B.; Chen, H.; Hou, Y.; et al. Passivation of the buried interface via preferential crystallization of 2D perovskite on metal oxide transport layers. *Adv. Mater.* **2021**, *33*, e2103394.
24. Yang, X.; Li, L.; Wu, J.; et al. Optimizing vertical crystallization for efficient perovskite solar cells by buried composite layers. *Sol. RRL* **2021**, *5*, 2100457.
25. Xu, Y.; Xiong, S.; Jiang, S.; et al. Synchronous modulation of defects and buried interfaces for highly efficient inverted perovskite solar cells. *Adv. Energy Mater.* **2022**, *13*, 2203505.
26. Wei, K.; Deng, J.; Yang, L.; et al. A core@dual-shell nanostructured SnO_2 to modulate the buried interfaces toward stable perovskite solar cells with minimized energy losses. *Adv. Energy Mater.* **2022**, *13*, 2203448.
27. Yang, X.; Luo, D.; Xiang, Y.; et al. Buried interfaces in halide perovskite photovoltaics. *Adv. Mater.* **2021**, *33*, e2006435.
28. Chen, S.; Xiao, X.; Chen, B.; et al. Crystallization in one-step solution deposition of perovskite films: Upward or downward?. *Sci. Adv.* **2021**, *7*, eabb2412.
29. Onoda-Yamamuro, N.; Yamamuro, O.; Matsuo, T.; et al. P-T phase relations of $CH_3NH_3PbX_3$ (X = Cl, Br, I) crystals. *J. Phys. Chem. Solids* **1992**, *53*, 277.
30. Baikie, T.; Fang, Y.; Kadro, J.M.; et al. Synthesis and crystal chemistry of the hybrid perovskite $CH_3NH_3PbI_3$ for solid-state sensitised solar cell applications. *J. Mater. Chem. A* **2013**, *1*, 5628.
31. Saidi, W.A.; Choi, J.J. Nature of the cubic to tetragonal phase transition in methylammonium lead iodide perovskite. *J. Chem. Phys.* **2016**, *145*, 144702.
32. Soe, C.M.; Stoumpos, C.C.; Harutyunyan, B.; et al. Room temperature phase transition in methylammonium lead iodide perovskite thin films induced by hydrohalic acid additives. *ChemSusChem* **2016**, *9*, 2656.
33. Wang, Q.; Lyu, M.; Zhang, M.; et al. Transition from the tetragonal to cubic phase of organohalide perovskite: the role of chlorine in crystal formation of $CH_3NH_3PbI_3$ on TiO_2 Substrates. *J. Phys. Chem. Lett.* **2015**, *6*, 4379.
34. Palazon, F.; Perez-Del-Rey, D.; Danekamp, B.; et al. Room-temperature cubic phase crystallization and high stability of vacuum-deposited methylammonium lead triiodide thin films for high-efficiency solar cells. *Adv. Mater.* **2019**, *31*, e1902692.
35. Tie-Ying, Y.; Wen, W.; Guang-Zhi, Y.; et al. Introduction of the X-ray diffraction beamline of SSRF. *Nucl. Sci. Tech.* **2015**, *25*, 5.
36. Saini, I.; Rozra, J.; Chandak, N.; et al. Tailoring of electrical, optical and structural properties of PVA by addition of Ag nanoparticles. *Mater. Chem. Phys.* **2013**, *139*, 802.
37. Kavadiya, S.; Strzalka, J.; Niedzwiedzki, M.; et al. Crystal reorientation in methylammonium lead iodide perovskite thin film with thermal annealing. *J. Mater. Chem. A* **2019**, *7*, 12790.
38. Jacobsson, T.J.; Schwan, L.J.; Ottosson, M.; et al. Determination of thermal expansion coefficients and locating the temperature-induced phase transition in methylammonium lead perovskites using X-ray diffraction. *Inorg. Chem.* **2015**, *54*, 10678.
39. Wei, Q.; Liang, H.; Haruta, Y.; et al. From tetragonal to cubic: perovskite phase structure evolution for high-performance solar cells. *Sci. Bull.* **2023**, *68*, 141–145.